Ultrasound in Med. & Biol., Vol. 49, No. 3, pp. 875–888, 2023

0301-5629/$ - see front matter

https://doi.org/10.1016/j.ultrasmedbio.2022.11.014

● *Original Contribution*

# LATERAL M-MODE: ULTRASOUND VISUALIZATION OF DISPLACEMENT ALONG LONGITUDINAL DIRECTION AT INTIMA–MEDIA COMPLEX

SHOHEI MORI,* MOTOTAKA ARAKAWA,*,† and HIROSHI KANAI*,†

* Graduate School of Engineering, Tohoku University, Sendai, Japan; and † Graduate School of Biomedical Engineering, Tohoku University, Sendai, Japan

(*Received* 29 *April* 2022; *revised* 9 *November* 2022; *in final form* 19 *November* 2022)

**Abstract—Quantification of the dynamics of the carotid artery wall is useful in evaluating arteriosclerosis and atherosclerosis. As the carotid artery wall moves not only in the radial direction but also in the longitudinal direction, longitudinal movement should be considered in the analysis of the dynamic properties of the carotid artery wall. In this study, we propose a "lateral M-mode" method for visualizing the longitudinal movement of the intima–media complex (IMC). For the lateral M-mode, we set the target line in the longitudinal direction along the IMC and visualize the signals on the target line frame-by-frame by correcting the position of the target line along the radial displacement estimated by the phased tracking method. Differentiating the envelope signals between consecutive ultrasound beams was effective in visualizing the lateral movement of the IMC. The precision of the longitudinal displacement of the IMC estimated using the conventional block-matching method was validated by comparing it with the lateral M-mode. Because the conventional M-mode sequence plays an important role in evaluation of the dynamics of various tissues, the proposed "lateral M-mode" contributes to a detailed understanding of vascular dynamics and the development of diagnostic methods for vascular diseases. (E-mail: mori@tohoku.ac.jp)** 

***Key Words:*** **Ultrasound, Arteriosclerosis, Atherosclerosis, Intima–media complex, Longitudinal motion, Lateral M-mode, Block matching.**

## INTRODUCTION

The characteristics and mechanical properties of the carotid artery are useful in diagnosing arteriosclerosis and atherosclerosis (Grobbee and Bots 1994; Wada et al. 1994; Catalano et al. 2011; Boesen et al. 2015). Ultrasound diagnostic apparatus is a powerful tool for disease diagnosis because of its non-invasiveness and real-time performance. The intima–media complex (IMC) thickness (IMT) measured from the B-mode image is a common indicator of the tissue characteristics of the carotid artery wall (Grobbee and Bots 1994; Stein et al. 2008). Pulse wave velocity (PWV) is an indicator of arterial wall stiffness (Bramwell and Hill 1922). Several studies have used ultrasound to measure PWV (Avolio et al. 1983; Benthin et al. 1991; Lehmann et al. 1992, 1993; Kanai et al. 1994; Eriksson et al. 2002; Luo et al. 2012; Ito et al. 2018; Nagaoka and Hasegawa 2020). In some of these studies, PWV has been estimated from the ultrasonically measured displacement of the carotid artery wall in the radial direction caused by the propagation of pulse waves (Benthin et al. 1991; Kanai et al. 1994; Eriksson et al. 2002; Luo et al. 2012; Ito et al. 2018; Nagaoka and Hasegawa 2020).

To evaluate mechanical properties, measurement methods for strain (Swillens et al. 2012), elasticity (Kanai et al. 2003; Hasegawa et al. 2004; Couade et al. 2010; Ramnarine et al. 2014; Salles et al. 2015) and viscoelasticity (Zhang et al. 2005; Arakawa et al. 2019; Saito et al. 2020; Shoji et al. 2021) of the arterial wall have been proposed. With these methods, radial and/or longitudinal displacements of the arterial wall are measured to estimate each parameter. The luminal surface roughness of IMC has also been studied as an indicator (Schmidt-Trucksäss et al. 2003; Cinthio et al. 2011; Kitamura et al. 2012; Nagai et al. 2014; Pozza et al. 2016). Kitamura et al. (2012) and Nagai et al. (2014) proposed a method for measuring ultrasonically the luminal surface roughness of the carotid artery wall in micron order, wherein the longitudinal displacement of the IMC caused by pulsation is used to consider the

Address correspondence to: Department of Electronic Engineering, Graduate School of Engineering, Tohoku University, Aramaki-aza-Aoba 6-6-05, Sendai 980-8579, Japan. E-mail: mori@tohoku.ac.jp

heterogeneity of the speed of sound in the ultrasound propagation medium from the skin to the carotid artery. In this method, accurate measurement of the longitudinal displacement of the IMC is essential.

Accurate measurement of the displacement of the arterial wall in the radial direction (*i.e.,* ultrasound beam direction) can be achieved using a phase-based velocity estimator (Kanai et al. 1996; Hasegawa et al. 1998; Rabben et al. 2002; Swillens et al. 2012; Pozza et al. 2016; Akiyama et al. 2021). However, accurate measurement of IMC displacement in the longitudinal direction is difficult in the early stage of arteriosclerosis because the thickness and acoustic properties of the IMC are almost similar along the longitudinal direction, and the difference in the envelope of the received ultrasound radiofrequency (RF) signals in the longitudinal direction is small. To overcome these difficulties, several studies have been conducted to estimate the longitudinal displacement of the carotid artery wall, as summarized by Rizi et al. (2020). These studies have applied a block matching-based approach (Persson et al. 2002; Golemati et al. 2003; Cinthio et al. 2005, 2006, 2007; Zahnd et al. 2011; Idzenga et al. 2012; Yli-Ollila et al. 2013; Tat et al. 2016; Au et al. 2017, 2019), an approach using the spatial phase information (Nilsson et al. 2013) and a 2-dimensional (2D) cross-spectrum approach in the frequency domain (Salles et al. 2015).

Although numerous techniques for estimating the longitudinal displacement of the carotid arterial wall have been studied and validated by simulations, phantom experiments and reproducibility evaluations in *in vivo* measurements, it is still difficult to confirm the actual precision of the estimated longitudinal displacement in *in vivo*. One of the reasons may be the non-existence of a method visualizing the longitudinal movement, whereas the precision of the radial displacement measurement can be confirmed by comparing it with the M-mode image. The development of a method for visualization of longitudinal movement contributes not only to the validation of the accuracy of the longitudinal displacement estimation but also to the easy observation of the longitudinal wall motion by clinicians, as well as the use of conventional M-mode imaging for the observation of radial wall motion.

To visualize the longitudinal movement of the IMC, we focused on anatomic M-mode imaging (Strotmann et al. 1999) used in the field of echocardiography. An anatomic M-mode can set the target line for M-mode imaging in an arbitrary direction, as shown in Figure 1a; therefore, the displacement (A) along the target line can be visualized, as shown in Figure 1b. In this anatomical M-mode sequence, the target line is fixed at the same position throughout the frames, similar to the conventional M-mode imaging.

In several cases, however, the object moves in 2-D directions, such as displacements (A) and (B), as shown in Figure 1a. In such cases, the position of the target line should be corrected along the displacement (B). This necessity was suggested by Carerj et al. (2003), but it was not implemented.

In this study, we proposed a method for visualization of the longitudinal displacement (A) of the IMC as "lateral M-mode," as shown in Figure 1c and 1d. To visualize longitudinal displacement (A), the target line was set along the longitudinal direction, as shown in Figure 1c, based on anatomical M-mode imaging. Because the IMC moves in both the radial and longitudinal directions, as shown in Figure 1c, the position of the target line should be corrected along the radial displacement (B) of the IMC. We applied the proposed lateral M-mode imaging method to validate the precision of the longitudinal displacement estimated using the conventional block-matching method.

## METHODS

### *Principle: Setting the target line at the 0th frame for lateral M-mode imaging*

Figure 2a illustrates a schematic of the B-mode image of the posterior wall, and Figure 2b shows the actual B-mode image obtained for a healthy individual in his twenties. The objective of the following procedure is to determine the depth of the target line, $z_0(m)$, on the $m$th beam at the 0th frame for the early stage of arteriosclerosis because it is difficult to estimate the longitudinal displacement in the early stage, as described in the Introduction. To determine $\{z_0(m)\}$ as shown in Figure 2a, we set the depths $\{z_{b1}(m)\}$ and $\{z_{b2}(m)\}$ to include only the signal from the IMC, as follows.

The arterial wall comprises intima, media and adventitia, as shown in Figure 2a. At the interface between the lumen and intima, the ultrasound is strongly scattered/reflected; therefore, a high-brightness region with a pulse length is observed in the B-mode image. Because the intima and media have similar acoustic properties, ultrasound is not scattered inside the IMC. Thus, if the IMC is thicker than the pulse length, a low-brightness region is observed on the adventitia side of the IMC. Thereafter, the ultrasound is strongly scattered/reflected at the interface between the media and adventitia, and a high-brightness region is observed at the adventitia.

The boundary depths $\{z_{b1}(m)\}$ between the lumen and intima are determined based on threshold processing, as shown in Figure 2b. First, the region $\{z|\ z_1 \le z \le z_2\}$, including both the lumen and IMC of the posterior wall, was manually assigned. Thereafter, the shallowest depth $z_{b1}(m)$ where the amplitude of the envelope is larger than the threshold $th$ is determined as the boundary depth as

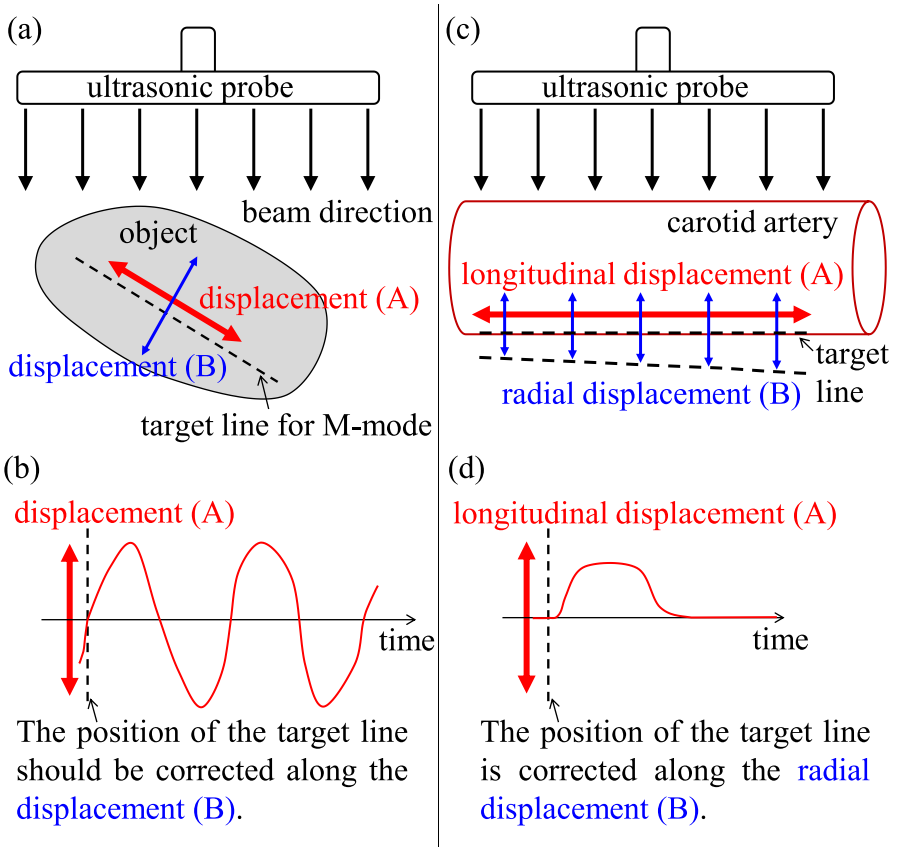


Fig. 1. (a) Schematic of measurement configuration for anatomic M-mode imaging and (b) the displacement (A) visualized in the anatomic M-mode imaging. (c) Schematic of measurement configuration for the carotid artery and (d) longitudinal displacement (A) visualized in the proposed lateral M-mode imaging.

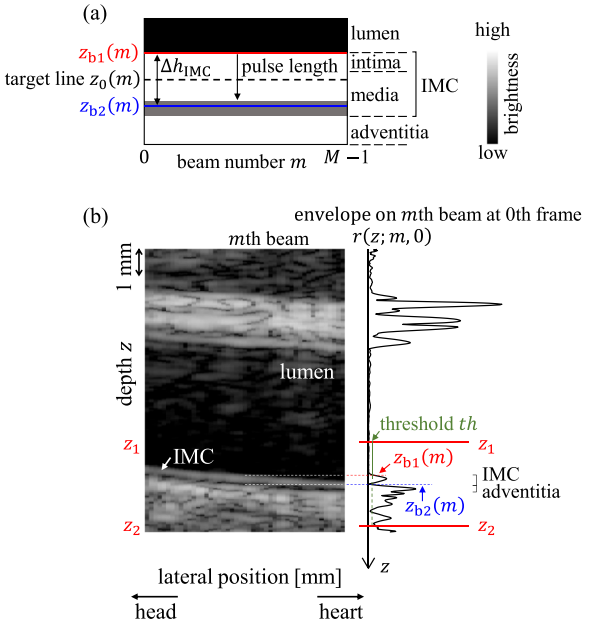


Fig. 2. (a) Schematic of the B-mode image of the posterior wall. (b) Example of a set of depths, $\{z_{b1}(m)\}$ and $\{z_{b2}(m)\}$, of the boundaries of the intima−media complex (IMC).

$$z_{b1}(m) = \min_z \left\{ \arg_z \{ r(z;m,0) \geq th \} \right\}, \quad (m = 0, \ldots, M-1) \tag{1}$$

where $r(z;m,n)$ denotes the envelope of the RF signal on the $m$th beam at the $n$th frame, and $M$ denotes the total number of ultrasound beams. This threshold processing was applied to each ultrasound beam independently for the 0th frame.

The boundary depths $\{z_{b2}(m)\}$ are set at the local minimum depths of the envelope inside the IMC, as shown in Figure 2a and 2b, to exclude the large signals from the adventitia that exhibits different movement from the IMC (Cinthio et al. 2006). However, the envelope at the depth of the local minimum is easily affected by background noise. To increase the signal-to-noise ratio, the envelopes measured by M ultrasound beams were averaged assuming that the thickness of the IMC was almost the same in the longitudinal direction in the early stage of arteriosclerosis.

In the actual case, the ultrasound probe surface can incline in the longitudinal direction of the carotid artery, as shown in Figure 3a and 3b. Thus, the inclination is corrected by $z_{b1}(m)$ by introducing $z' = z - z_{b1}(m)$, as shown in Figure 3b and 3c. The corrected envelope signal $r'(z';m)$ on the $m$th beam is defined at the 0th frame as

$$r'(z';m) = r(z' + z_{b1}(m); m, 0). \quad (2)$$

Subsequently, the corrected envelope signals $\{r'(z';m)\}$ are averaged (Fig. 3c, 3d), as

$$\overline{r'(z')} = \frac{1}{M}\sum_{m=0}^{M-1} r'(z';m). \quad (3)$$

The thickness of the IMC region, $\Delta h_{IMC}$, is thereafter determined as the shallowest local minimum depth of $\overline{r'(z')}$ as

$$\Delta h_{IMC} = \min_{z'}\{\arg_{z'}\{\overline{r'(z')} < \overline{r'(z'-\delta z)} \cap \overline{r'(z')} < \overline{r'(z'+\delta z)}\}\}, \quad (4)$$

where $\delta z$ denotes the sampling interval in the depth direction. Finally, the depth $z_{b2}(m)$ is determined as

$$z_{b2}(m) = z_{b1}(m) + \Delta h_{IMC}, \ (m = 0, \ldots, M-1). \quad (5)$$

Thus, the depths $\{z_{b1}(m)\}$ and $\{z_{b2}(m)\}$ were determined for each beam $m$ as shown in Figure 3e.

Using the depths $\{z_{b1}(m)\}$ and $\{z_{b2}(m)\}$, the depths of the target line for lateral M-mode imaging at the 0th frame, $\{z_0(m)\}$, were defined, as shown in Figure 3e:

$$z_0(m) = \frac{z_{b1}(m) + z_{b2}(m)}{2}. \quad (6)$$

*Principle: Lateral M-mode imaging*

The objective is to visualize the longitudinal displacement (A) of the IMC, as shown in Figure 1c and 1d; therefore, the target line for lateral M-mode imaging at the 0th frame is set at depths $\{z_0(m)\}$ along the longitudinal direction of the IMC by eqn (6). Because the IMC moves in both the longitudinal and radial directions

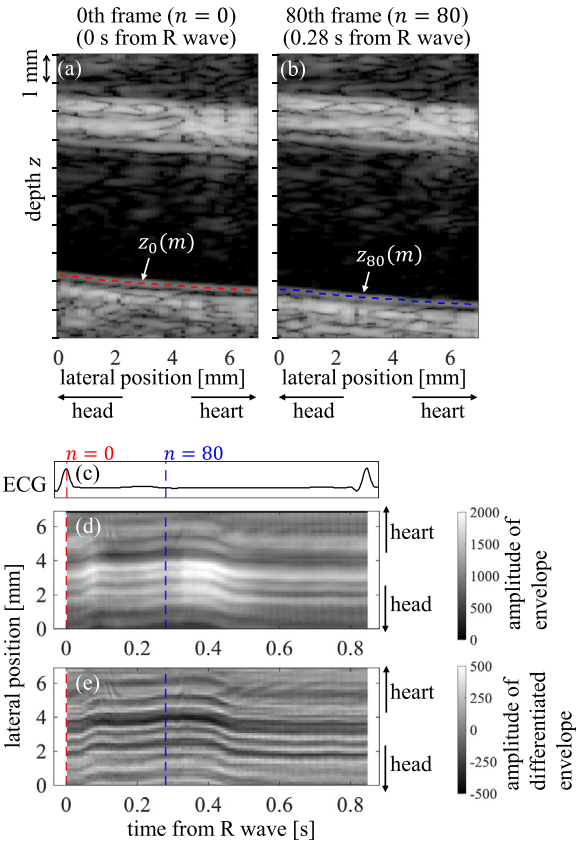


Fig. 4. Example of the longitudinal movement visualization of the intima–media complex (IMC) on the lateral M-mode. (a, b) B-mode images in the (a) 0th and (b) 80th frames. (c) Electrocardiogram (ECG). (d, e) Lateral M-mode: proposed visualized images of the longitudinal movement of the IMC with the use of the (d) amplitude of the envelope and (e) amplitude of the differentiated envelope.

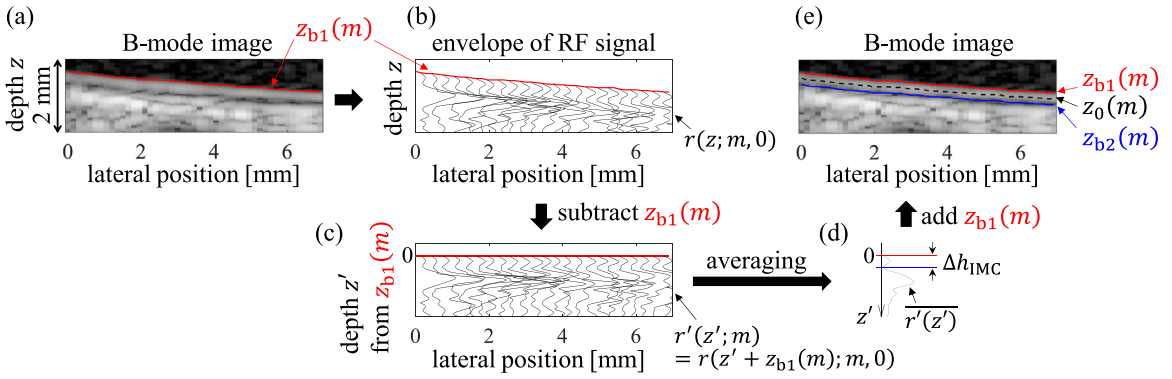


Fig. 3. Schematic of the set of the depths of the target line at the 0th frame, $\{z_0(m)\}$, for lateral M-mode imaging.

by pulsation, as shown in Figure 1c, the position of the target line is corrected frame-by-frame along the radial displacement (B) as

$$z_{n+1}(m) = z_0(m) + \frac{1}{FR}\sum_{k=0}^{n} v_{\mathrm{d}}(k;m), \tag{7}$$

where $z_n(m)$ denotes the depth of the target line on the $m$th beam at the $n$th frame, $FR$ denotes the frame rate and $\hat{v_{\mathrm{d}}}(n;m)$ denotes the velocity in the radial direction between the $n$th and $(n+1)$th frames estimated on the $m$th beam, which was obtained using a multifrequency-phased tracking method (Obara et al. 2021) with a window length of $\Delta h_{\mathrm{IMC}}$. When $z_n(m)$ is not the integral multiple of sampling interval $\delta z$, it is rounded off to be the closest integral multiple of $\delta z$.

Subsequently, the signals $\{s_n(z_n(m);m)\}$ on the target line $\{z_n(m)\}$ in the $n$th frame are visualized as the lateral M-mode, where we compare the use of two different types of signals for $s_n(z;m)$: the conventional use of an envelope, as

$$s_n(z;m) = r(z;m,n), \tag{8}$$

and the use of a differentiated envelope between consecutive ultrasound beams to emphasize the difference in amplitude in the longitudinal direction, as

$$s_n(z;m) = r(z;m+1,n) - r(z;m,n). \tag{9}$$

Finally, the amplitudes of the signals $\{s_n(z_n(m);m)\}$ on the target line $\{z_n(m)\}$ are converted to 8-bit grayscale pixel values $\{I_{\mathrm{L}}(n,m)\} \in [0,\ 255]$ as

$$I_{\mathrm{L}}(n,m) = \begin{cases} 0 & s_n(z_n(m);m) < ar_1 \\ \lfloor 255 \cdot \dfrac{s_n(z_n(m);m) - ar_1}{ar_2 - ar_1} + 0.5 \rfloor & ar_1 \le s_n(z_n(m);m) < ar_2 \\ 255 & s_n(z_n(m);m) \ge ar_2 \end{cases}, \tag{10}$$

where $\lfloor \cdot \rfloor$ denotes an operation of the floor function and $[ar_1, ar_2]$ denotes the visualized amplitude range of the signal $s_n(z_n(m);m)$. The pixel values $I_{\mathrm{L}}(n,m)$ of 0 and 255 indicate *black* and *white*, respectively, and $\{I_{\mathrm{L}}(n,m)\}$ is visualized as a lateral M-mode image with frame $n$ on the horizontal axis and beam number $m$ on the perpendicular axis.

Figure 4 shows an example of lateral M-mode imaging. Figure 4a and 4b show the depths of the target line at the 0th frame, $\{z_0(m)\}$, and at the 80th frame, $\{z_{80}(m)\}$, respectively. The target line moved in the radial direction, as shown in Figure 4a and 4b. Figure 4c shows the electrocardiogram (ECG) waveform. Figure 4d and 4e show the lateral M-mode images obtained using eqns (8) and (9), respectively. In Figure 4d and 4e, $[ar_1, ar_2]$ was set as $[0,\ 2000]$ and $[-500,\ 500]$, respectively. The longitudinal movement of the IMC is visualized as a change in equal pixel values in the upward and downward directions, which correspond to the rightward and leftward directions in the B-mode image, that is, the movements toward the heart and head sides, respectively.

*Measurement configuration*

The right common carotid arteries in three healthy young volunteers, namely, A, B and C in their early twenties, and the older healthy volunteer D in his early fifties (all volunteers were male with no obesity), were measured using an ultrasound diagnostic apparatus. The *in vivo* measurements used in this study were approved by the ethics committee of the Graduate School of Engineering at Tohoku University (No. 19A-5). All the participants agreed to participate in the study.

A linear probe (UST-5410, Hitachi-Aloka-Medical Ltd., Tokyo, Japan) connected to an ultrasound diagnostic apparatus (SSD-6500, Hitachi-Aloka-Medical Ltd.) was used. The diagnostic apparatus was customized to output the raw beamformed RF signals. The acquired raw beamformed RF signals were loaded and analyzed offline using a program developed by our group that was operated using MATLAB R2020b (The MathWorks Inc., Natick, MA, USA). Center frequency, sampling frequency and beam intervals of 7.5 MHz, 40 MHz and 150 $\mu$m, respectively, were used. The number of ultrasound beams, $M$, was set as 47. The frame rate was set at 286 Hz, at which the maximum instantaneous velocity of approximately 14 mm/s can be measured without aliasing, under the condition the transmitted frequency was 7.5 MHz (the wavelength is approximately 0.2 mm), which was empirically sufficient for measuring the radial velocity of the carotid artery wall. The electrocardiogram (ECG) was simultaneously measured for lead II using the three-point lead method.

*Estimation of longitudinal displacement of the IMC by a conventional block-matching method*

The proposed lateral M-mode was applied to validate the estimated longitudinal movement of the IMC using a conventional block-matching method.

In this study, the conventional block-matching method based on normalized cross-correlation (Golemati et al. 2003) was used to estimate the longitudinal displacement between consecutive frames, $\Delta x_n$, of the IMC by maximizing the normalized cross-correlation $C_n$ between consecutive frames. The longitudinal position

$x_n$ in the $n$th frame is tracked as

$$x_{n+1} = x_0 + \sum_{k=0}^{n} \Delta x_k, \tag{11}$$

where $x_0$ denotes the center position of the correlation kernel at the 0th frame (time of the first R-wave).

Because the lateral sampling interval $\delta x$, which was 150 $\mu m$ in this study, is larger than the longitudinal displacement of the IMC between frames (Kitamura et al. 2012), the normalized cross-correlation function $C_n$ was interpolated using reconstructive interpolation (Céspedes et al. 1995) such that the interpolated sampling intervals became approximately 1 μm in both the depth and lateral directions.

When updating the depth of the correlation kernel from the $n$th frame to the $(n+1)$th frame, the tracked depth $z_n(m)$ obtained with the multifrequency phased tracking method in eqn (7) was used instead of the tracked depth obtained with the block-matching method because the phase of the RF signal can be effectively used in the depth direction.

The differentiated envelope between the consecutive ultrasound beams defined in eqn (9) was used in the block-matching method to emphasize the difference in the envelope in the longitudinal direction. The width of the correlation kernel was empirically determined as 2.4 mm (17 beams). The center depth of the correlation kernel on the $m$th beam was set at the depth of the target line $z_n(m)$. The height of the correlation kernel was set to $\Delta h_{\mathrm{IMC}}$ which was determined by eqn (4); 0.35 mm for participants A, B and D, and 0.39 mm for participant C. The height of the correlation kernel was fixed throughout the cardiac cycle.

Figure 5a and 5b show examples of the conventional B-mode image and the image of the differentiated envelope between consecutive beams, respectively, at the 0th frame (the time of the first R-wave). The *red parallelograms* in Figure 5a and 5b show an example of the position of the correlation kernel at the 0th frame for the block-matching method. Although the brightness of the IMC was almost homogeneous in the longitudinal direction, as shown in Figure 5a, the pattern of positive values (high brightness) and negative values (low brightness) observed in Figure 5b can be effectively used in the block-matching method.

Figure 5c and 5d show the spatial distributions of the normalized cross-correlation $C_n$ between the 0th and 1st frames, calculated for the envelope $r(z;m,n)$ and for the differentiated envelope $r(z;m+1,n) - r(z;m,n)$, respectively. As shown in Figure 5c, large correlation values were observed along the longitudinal direction; therefore, estimating the displacement of the IMC may become unstable. In contrast, in Figure 5d, the spatial distribution of the correlation value changes significantly, and its large value is concentrated at a single position. Figure 5e shows the tracking results for the correlation kernel set shown in Figure 5a and 5b. The results were superimposed onto a lateral M-mode image. The *blue* and *red lines* represent the results using envelope $r(z;m,n)$ and differentiated envelope $r(z;m+1,n) - r(z;m,n)$, respectively, in the block-matching method. In the result obtained using the envelope (*blue*), the tracked position gradually deviated in the heart direction compared with the trajectory observed in the lateral M-mode image. These examples indicate that the use of a differentiated envelope is superior to the simple use of an envelope for estimating the longitudinal displacement of the IMC using the correlation-based block-matching method.

*Evaluation of validity of tracking results using lateral M-mode image*

We evaluated the validity of the estimated longitudinal displacement using the block-matching method by comparing the result with the trajectory observed in the lateral M-mode image. When the estimated displacement corresponds to the trajectory on the lateral M-mode image, the pixel values of the lateral M-mode image along the estimated displacement become constant because the same point in the IMC is tracked throughout the cardiac cycle.

Thus, we evaluated the standard deviation $SD(x_0)$ of the pixel values of the lateral M-mode image along the estimated longitudinal position $x_n$, as

$$SD(x_0) = \sqrt{\frac{1}{N}\sum_{n=0}^{N-1}\left\{I_{\mathrm{L,ip}}\left(n,\ \lfloor \frac{x_n}{\delta x_{\mathrm{ip}}} + 0.5 \rfloor\right) - \mathrm{E}_n\left[I_{\mathrm{L,ip}}\left(n,\ \lfloor \frac{x_n}{\delta x_{\mathrm{ip}}} + 0.5 \rfloor\right)\right]\right\}^2}, \tag{12}$$

where $\mathrm{E}_n[\cdot]$ denotes the average operation for $n = 0, 1, \cdots, N-1$; $x_n$ denotes the estimated longitudinal position at the $n$th frame, obtained using eqn (11), and $x_0$ denotes the lateral position of the correlation kernel for block matching in the 0th frame; $I_{\mathrm{L,ip}}(n, m_{\mathrm{ip}})$ denotes the interpolated lateral M-mode image of $I_{\mathrm{L}}(n,m)$ in eqn (10), which was interpolated along the $m$-direction (*i.e.*, the perpendicular direction of the lateral M-mode image), $m_{\mathrm{ip}}$ denotes the interpolated beam number and $\delta x_{\mathrm{ip}}$ denotes the interpolated lateral sampling interval of the B-mode image (*i.e.*, the perpendicular sampling interval of the lateral M-mode image). $\delta x_{\mathrm{ip}}$ was set as 1 μm, which is the same as the interpolation for the correlation function $C_n$ in the block-matching method. Here, similar to the block-matching method, interpolation along the $m$-direction was used because the instantaneous

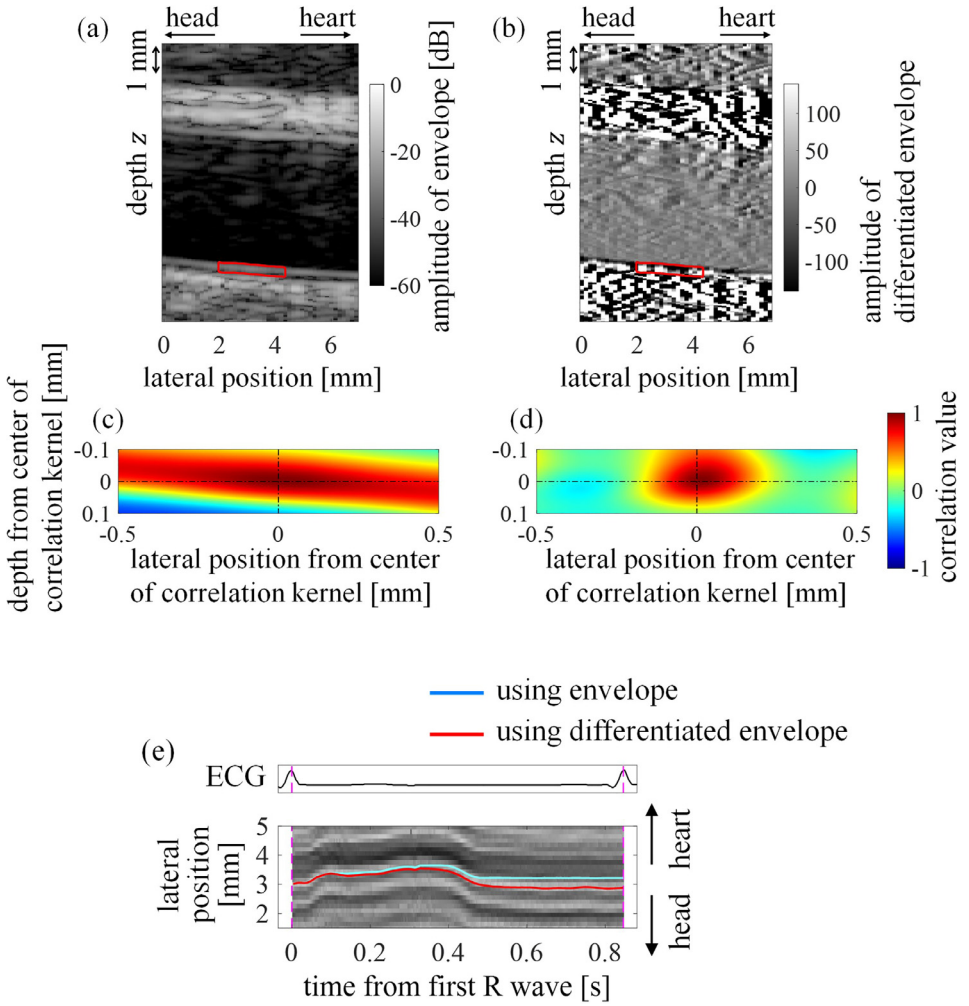


Fig. 5. (a) Conventional B-mode image and (b) image of the differentiated envelope between consecutive ultrasound beams at the 0th frame (time of R-wave) for participant A. (c, d) Normalized cross-correlations between the 0th and 1st frames where the correlation kernel was set as a *red parallelogram* on (a) and (b), respectively. (e) Estimated results of the longitudinal displacement of the intima−media complex (IMC) by the block-matching method, superimposed on the lateral M-mode image. The result using the differentiated envelope in the block-matching method is plotted as a *blue line* and the result using the simple envelope is plotted as a *red line*.

displacement $\Delta x_n$ between consecutive frames was smaller than the sampling interval of $\delta x = 150$ μm. The small value of $SD(x_0)$ indicates that the difference in the pixel values of the lateral M-mode image along the estimated longitudinal displacement is small; that is, the estimated displacement by the block-matching method corresponds to the trajectory observed in the lateral M-mode image obtained using an approach different from the block-matching method.

## RESULTS

*Lateral M-mode imaging*

Figure 6a−d show conventional B-mode images for participants A−D, respectively. The *red* and *blue solid lines* represent the boundary depths of the IMC region, $\{z_{b1}(m)\}$ and $\{z_{b2}(m)\}$, determined using eqns (1) and (5), respectively, and the *black dashed line* represents the depths of the target line at the 0th frame, $\{z_0(m)\}$, determined using eqn (6). For all participants, $\{z_{b1}(m)\}$ and $\{z_{b2}(m)\}$ were determined to include only the IMC, and the target line at the 0th frame was precisely assigned to the depth of the IMC.

Figure 7i−iii show the ECG, lateral M-mode images obtained using the amplitude of the envelope in eqn (8) and the lateral M-mode image using the amplitude of the differentiated envelope in eqn (9), respectively. Figure 7a−d show the results for participants A−D, respectively. Lateral M-mode images of two consecutive cardiac cycles are shown. As shown in the

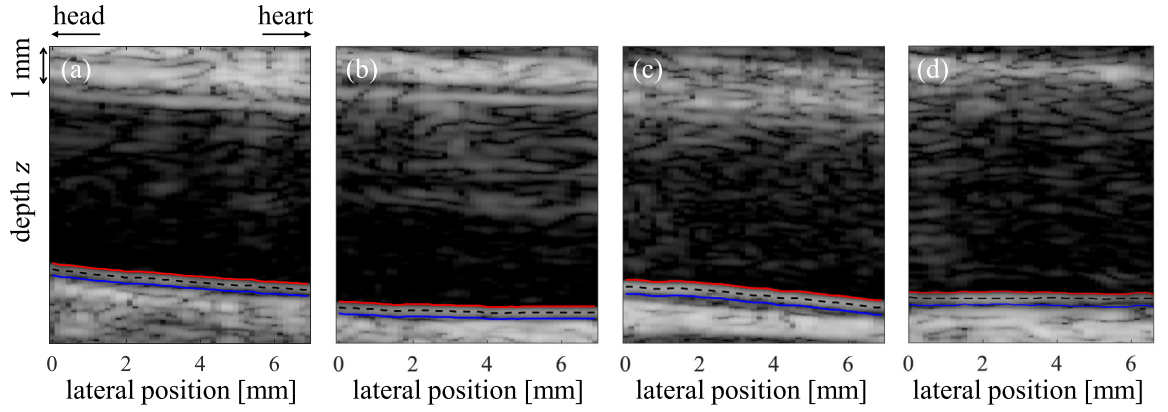


Fig. 6. Detected boundary depths $\{z_{b1}(m)\}$ (*red solid line*) and $\{z_{b2}(m)\}$ (*blue solid line*) and determined depths of the target line at the 0th frame, $\{z_0(m)\}$ (*black dashed line*). (a–d) Participants A–D, respectively.

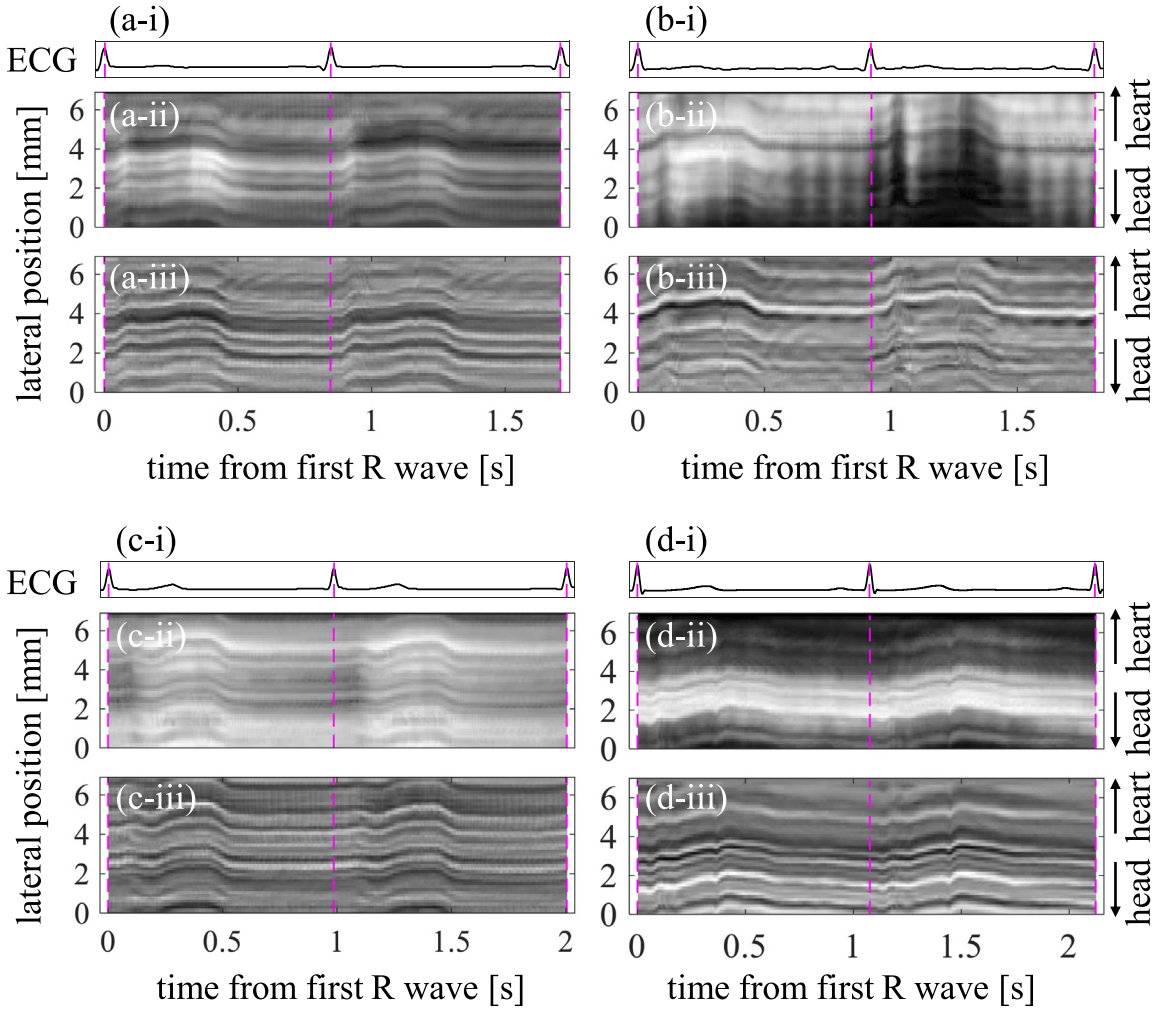


Fig. 7. (i) Electrocardiogram (ECG). (ii) Lateral M-mode images with the use of the amplitude of the envelope. (iii) Lateral M-mode images with the use of the amplitude of the differentiated envelope. (a–d) Participants A–D, respectively.

longitudinal movement in the lateral M-mode, the IMC moved to the heart side and thereafter returned to the head side for all participants.

In Figure 7ii, the lateral M-mode exhibits a global change in brightness along the time direction. For instance, in Figure 7c-ii, the amplitudes of the envelope became large from 0.15 to 0.5 s, compared with that from 0 to 0.15 s, regardless of the lateral positions. Moreover, as shown in Figure 7b-ii, the amplitude of the envelope significantly decreased in the second cardiac cycle. In contrast, the differentiated envelope in Figure 7iii exhibits only a brightness change along the longitudinal direction (perpendicular direction in Figure 7iii), which reflects the longitudinal movement of the IMC. Thus, for the proposed lateral M-mode, a differentiated envelope was suitable for observing the longitudinal movement of the IMC.

*Validation for estimated 2-D displacements*

To demonstrate the use of the proposed lateral M-mode imaging method, the results of the longitudinal displacements estimated using the conventional block-matching method were superimposed on the lateral M-mode image. Figure 8i–iii show the ECG, the conventional M-mode image in the radial direction and the proposed lateral M-mode image, respectively. Figure 8a–d show the results for participants A–D, respectively. The differentiated envelope in eqn (9) was used for lateral M-mode imaging. The depth of the target line, $z_n(m = 24)$, on the 24th beam (center beam) is plotted in Figure 8ii using the *yellow line*. The longitudinal position $x_n$ tracked by the block-matching method for the differentiated envelope is plotted in Figure 8iii with *red*, *green* and *blue lines*. The different colors represent the results for the different center positions of the correlation kernel in the 0th frame (the time of the first R-wave) in the block-matching method.

The depth of the target line (yellow line), $z_n(m = 24)$, in Figure 8ii corresponds well to the trajectory observed in the conventional M-mode image. Similarly, the tracked longitudinal positions $x_n$ (*red*, *blue* and *green lines*) in Figure 8iii correspond well to the trajectories observed in the proposed lateral M-mode image for two consecutive cardiac cycles. Thus, the precision of the estimated longitudinal displacements was qualitatively confirmed by comparing them with the proposed lateral M-mode images.

To quantitatively evaluate the validity of the estimated longitudinal displacement by the block-matching method, the standard deviation $SD(x_0)$ for the pixel values in the lateral M-mode image was evaluated using eqn (12). The standard deviation $SD_{\mathrm{DE}}(x_0)$ obtained for the longitudinal displacement estimated using the differentiated envelope $r(z; m+1, n) - r(z; m, n)$ and the $SD_{\mathrm{E}}(x_0)$ for the longitudinal displacement estimated using the simple envelope $r(z; m, n)$ in the block-matching method were compared. The maximum value among the results for three different initial positions $x_0$ of the correlation kernel was evaluated. The maximum values obtained were 30 ($SD_{\mathrm{DE}}(x_0)$) versus 39 ($SD_{\mathrm{E}}(x_0)$) for participant A, 30 versus 88 for participant B, 17 versus 24 for participant C and 20 versus 39 for participant D, where the upper limit of the pixel value was 255, as defined by eqn (10). Thus, for all participants, the standard deviation $SD_{\mathrm{DE}}(x_0)$ obtained for the longitudinal displacement estimated using the differentiated envelope was less than the $SD_{\mathrm{E}}(x_0)$ for the longitudinal displacement estimated using the envelope. Determining the threshold of *SD* that guarantees the accuracy of the estimated displacement is part of our future study.

We observed the trajectory of the 2-D displacement from each of the three initial positions ($x_n - x_0$, $z_n - z_0$) of the IMC for four participants, as shown in Figure 8iv. In Figure 8iv, the positions at the time of the first R-wave are defined as $(0, 0)$, those at the time of the second R-wave as *circles* and those at the time of the third R-wave as *squares*. The trajectories in the first and second cardiac cycles are represented by *solid* and *dotted lines*, respectively.

In Figure 8iv, the results are shown to follow a similar trajectory between consecutive cardiac cycles, although with subtle differences. Moreover, the trajectory returned to its original position $(0, 0)$ after one cardiac cycle. The detailed 2-D trajectory differed by participant; however, the tendency of the trajectory was similar, particularly for participants A and C: (I) first, the IMC moved mainly in a radial direction by vessel dilatation; (II) this was followed by movement in a longitudinal direction toward the heart side; (III) thereafter the IMC moved mainly in a longitudinal direction toward the head side (returning movement); and (IV) finally returned to its original position by moving in a radial direction. This figure-of-eight pattern was also reported by Au et al. (2019), who measured it for young children under 10 y of age, although the detailed trajectories were different from the present results in Figure 8iv. Note that the right direction corresponds to the direction toward the head, and the upper direction corresponds to the deeper direction of the B-mode image in the coordinates for the 2-D trajectory reported by Au et al. (2019). These orientations were opposite to the directions in Figure 8iv. For participant B, a similar pattern was observed, although it was not as pronounced as compared with those for participants A and C. For participant D in his early fifties, the figure-of-eight pattern was not observed, as shown in Figure 8d-iv.

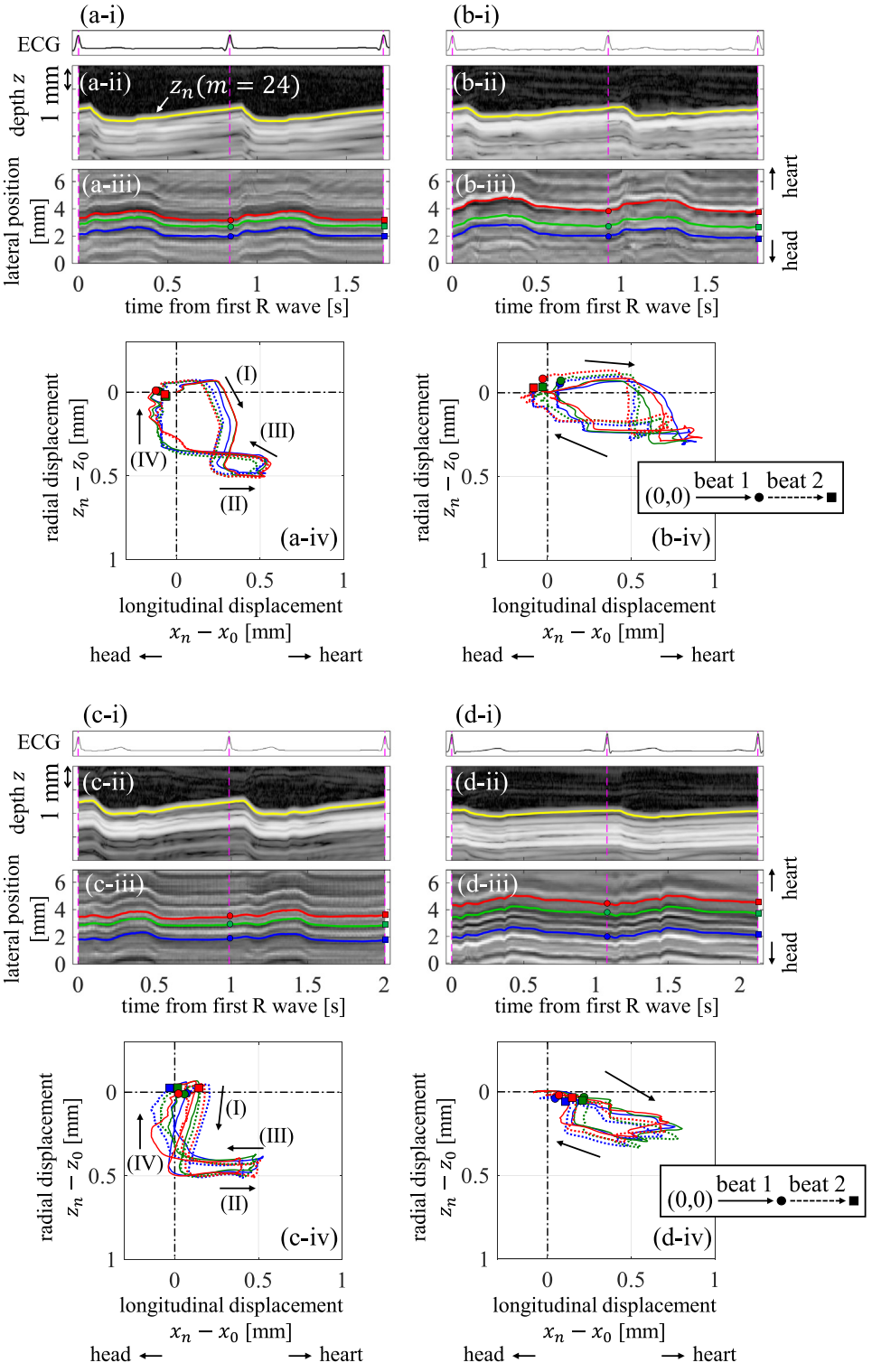


Fig. 8. (i) Electrocardiogram (ECG). (ii) Conventional M-mode image. (iii) Lateral M-mode image with the use of the amplitude of the differentiated envelope. (iv) Trajectories of 2-D displacements of the intima–media complex. (a–d) Participants A–D, respectively. The estimated depth of the target line, $z_n$ ($m = 24$), on the 24th beam (center beam) is represented by the *yellow line* in (ii). The longitudinal positions $x_n$ estimated by the conventional block-matching method at the three points are superimposed in (iii).

## DISCUSSION

In this study, lateral M-mode imaging, which visualizes the longitudinal movement of the IMC, is proposed.

As shown in Figure 6, the boundary depths of the IMC region, $\{z_{b1}(m)\}$ and $\{z_{b2}(m)\}$, were precisely determined to include only the IMC in all four healthy participants. This procedure aims mainly to exclude large signals from the adventitia because the movement of the adventitia differs from that of the IMC, as reported by Cinthio et al. (2006). Hence, the inclusion of the entire IMC in the ROI was not necessary for this study. Therefore, this method cannot guarantee whether the determined boundary is exactly the boundary between the media and adventitia, although it can stably exclude signals from the adventitia. Thus, when this method is applied to other applications such as IMT measurements, careful examination is required. The determination method for the IMC region was also developed by other groups, as summarized by Meiburger et al. (2022). A simple threshold approach was used in the present study to determine the boundary between the lumen and intima. The approach worked well for the measurements conducted in this study; however, the application of a more robust detection method proposed by other groups will improve the robustness of lateral M-mode imaging and displacement estimation by the block-matching method, particularly for less echogenic data in older and/or diseased participants. The robustness of the IMC boundary detection method may affect the robustness of the lateral M-mode imaging and longitudinal displacement estimation by the block-matching method; therefore, an evaluation of the robustness of each method is a topic for future work.

For the lateral M-mode, which visualizes the longitudinal movement of the IMC using eqn (10), a clear and sharp image was obtained by introducing a differentiated envelope between consecutive beams using eqn (9), as shown in Figure 7iii. There are several possible reasons for this finding. First, the difference in brightness in the longitudinal direction is emphasized by differentiating the envelopes between consecutive beams. Second, the global brightness change in the time direction (*i.e.,* the frame direction) was observed using eqn (8) (Fig. 7ii), but not with eqn (9) (Fig. 7iii), as described under Results section. The cause of this global brightness change in time direction remains unclear. However, this global brightness change appeared only in the time direction and not in the longitudinal direction, and was suppressed by differentiating the envelopes between consecutive beams (*i.e.*, differentiating in the longitudinal direction). Thus, only the brightness change caused by the longitudinal displacement of the IMC was emphasized, as shown in Figure 7iii.

For lateral M-mode imaging, only a 1-D phase-based estimator for the radial displacement was used. We discuss the computational capacity of the 1-D phase-based estimator used for lateral M-mode imaging and the 2-D block-matching method used for longitudinal displacement estimation. It is difficult to compare the detailed computational capacity because it depends on the algorithm used and the use/non-use of parallel processing. Therefore, we compared the dominant order of the number of multiplied operations used in each method.

In the 1-D multifrequency-phased velocity estimator (Obara et al. 2021), the dominant factor affecting computational capacity is the Fourier transform. Therefore, the dominant order of the number of multiplied operations is $L_d^2$ ($L_d$ is the window length in the radial direction) when a simple discrete Fourier transform is used.

In the 2-D block-matching method used for longitudinal displacement estimation, the dominant procedure affecting the computational capacity is the interpolation of the 2-D cross-correlation function $C_n$, which is required to estimate the sub-pixel displacement. In this study, $C_n$ was interpolated by factors of 20 in the depth direction and 150 in the lateral direction, to ensure that the interpolated sampling intervals were approximately 1 μm. The dominant order of the number of multiplied operations in the procedure for interpolation in the time domain is $(20L_d \times L_w) \times L_d^2$ (interpolation in the depth direction) + $(20L_d \times 150L_w) \times L_w^2$ (interpolation in the lateral direction).

In this study, $L_d$ was 19 for participants A, B and D, and 21 for participant C; and $L_w$ was 17 for all participants. Thus, under the present measurement condition, the 1-D velocity estimator used for lateral M-mode imaging can reduce the dominant order of the number of multiplied operations from $10^8$ (or $10^7$ when the interpolation is conducted in the frequency domain with the fast Fourier transform) to $10^2$, for each lateral position and frame, compared with the 2-D block-matching method used for the longitudinal displacement estimator.

By comparing the estimated longitudinal displacements of the IMC with the lateral M-mode image, we confirmed that the longitudinal displacement estimated by the block-matching method for the differentiated envelope corresponded well to the trajectory observed in the lateral M-mode image compared with the result using the simple envelope in the block-matching method. The lateral M-mode image is obtained using an approach different from the longitudinal displacement estimator (block-matching method in this study); that is, the lateral M-mode imaging is not affected by the longitudinal displacement estimator used. Thus, the lateral M-mode image may be effective in validating the longitudinal

displacement estimator and may contribute to the development of an accurate estimation method for the longitudinal movement of the IMC.

In the block-matching method used in this study, the height of the window was fixed throughout the cardiac cycle. However, Rafati et al. (2019) reported that the IMT of the common carotid artery changes by a maximum of approximately 125 μm in a cardiac cycle, which is a change of approximately 10%. Thus, adaptively changing the window height may improve tracking accuracy. Development of a more accurate method for estimating the longitudinal displacement of IMC is a future challenge.

The trajectories of the 2-D displacements in Figure 8 (a-iv to c-iv) for young healthy adults A, B and C in their early twenties differed by participant, although the shape of the trajectory exhibited a similar tendency. Differences in the measurement conditions, such as the pushing force of the probe, may affect the movement of the carotid artery wall. The trajectory of 2-D displacements for young healthy adults A, B and C in their early twenties exhibit the figure-of-eight pattern, which was also reported by Au et al. (2019) measured for children younger than 10 y of age. However, there were some differences between the trajectory waveforms obtained in this study and those reported by Au et al. (2019). Moreover, for older healthy adult D in his early fifties, the figure-of-eight pattern was not observed, as shown in Figure 8d-iv. As reported by Au et al. (2017), the waveforms of radial and longitudinal displacements of the carotid artery wall differ based on age. This is one of the prospective reasons for the aforementioned differences in the trajectories of the 2-D displacements. As the number of participants was limited in the present study, a detailed analysis of a large number of participants in different age groups, including the robustness evaluation for less echogenic data, is necessary for our future study.

In this study, we applied the proposed method only to the right common carotid artery; therefore, in future studies, we will examine the applicability of the method to other targets, such as the left common carotid artery and the right and left carotid sinuses.

In the present study, raw RF signals were used for lateral M-mode imaging; therefore, the proposed method needs to be implemented in the diagnostic apparatus by manufacturers as a new application for clinical use. To expand the application of the proposed lateral M-mode imaging, we will examine the method applicable to compressed data that can be acquired from the commercially used diagnostic apparatus by clinicians themselves.

## CONCLUSIONS

In this study, the "lateral M-mode" method is proposed for visualizing the longitudinal movement of the IMC. The lateral M-mode can be used for validation of the longitudinal displacement estimator. Moreover, we can observe the longitudinal movement of the IMC only from the lateral M-mode image, without estimating the longitudinal displacement. For lateral M-mode imaging, only a 1-D phase-based estimator with a low computational capacity is required; therefore, it may be implementable in clinical applications. As the conventional M-mode sequence plays an important role in evaluation of the dynamics of various tissues, the "lateral M-mode" proposed for visualization of the longitudinal movement of the IMC will contribute to the detailed understanding of vascular dynamics and the development of diagnostic methods for vascular diseases.

## DATA AVAILABILITY STATEMENT

The authors do not have permission to share data.

*Acknowledgments*—This study was supported in part by Japan Society for the Promotion of Science KAKENHI Grants 19KK0100 and 21K14166.

*Conflict of interest disclosure*—The authors declare that they have no competing interests.

## REFERENCES

Akiyama S, Mori S, Arakawa M, Kanai H. Accuracy verification in ultrasonic elasticity measurement within intima−media complex visible range using phantom experimental system. Jpn J Appl Phys 2021;60 SDDA07-1−SDDA07-7.

Arakawa M, Saito T, Mori S, Ohba S, Kobayashi K, Kanai H. Development of an ultrasonic probe to measure both radial arterial pressure and diameter change at the same position for early diagnosis of vascular endothelial function: Preliminary study. Sens Actuators A 2019;297 111487-1−111487-4.

Au JS, Valentino SE, McPhee PG, MacDonald MJ. Diastolic carotid artery longitudinal wall motion is sensitive to both aging and coronary artery disease status independent of arterial stiffness. Ultrasound Med Biol 2017;43:1906–1918.

Au JS, Proudfoot NA, Timmons BW, MacDonald MJ. Retrograde shift in carotid artery longitudinal wall motion after one-year follow-up in children. Atherosclerosis 2019;288:26–32.

Avolio AP, Chen SG, Wang RP, Zhang CL, Li MF, O'Rourke MF. Effects of aging on changing arterial compliance and left ventricular load in a northern Chinese urban community. Circulation 1983;68:50–58.

Benthin M, Dahl P, Ruzicka R, Lindström K. Calculation of pulse-wave velocity using cross correlation—Effects of reflexes in the arterial tree. Ultrasound Med Biol 1991;17:461–469.

Boesen ME, Singh D, Menon BK, Frayne R. A systematic literature review of the effect of carotid atherosclerosis on local vessel stiffness and elasticity. Atherosclerosis 2015;243:211–222.

Bramwell JC, Hill AV. The velocity of the pulse wave in man. Proc R Soc Lond B Biol Sci 1922;93:298–306.

Carerj S, Micari A, Trono A, Giordano G, Cerrito M, Zito C, Luzza F, Coglitore S, Arrigo F, Oreto G. Anatomical M-mode: An old-new technique. Echocardiography 2003;20:357–361.

Catalano M, Lamberti-Castronuovo A, Catalano A, Filocamo D, Zimbalatti C. Two-dimensional speckle-tracking strain imaging in the assessment of mechanical properties of carotid arteries: feasibility and comparison with conventional markers of subclinical atherosclerosis. Eur J Echocardiogr 2011;12:528–535.

Céspedes I, Huang Y, Ophir J, Spratt S. Methods for estimation of subsample time delays of digitized echo signals. Ultrason Imaging 1995;17:142–171.

Cinthio M, Ahlgren ÅR, Jansson T, Eriksson A, Persson HW, Lindström K. Evaluation of an ultrasonic echo-tracking method for measurements of arterial wall movements in two dimensions. IEEE Trans Ultrason Ferroelectr Freq Control 2005;52:1300–1311.

Cinthio M, Ahlgren ÅR, Bergkvist J, Jansson T, Persson HW, Lindström K. Longitudinal movements and resulting shear strain of the arterial wall. Am J Physiol Heart Circ Physiol 2006;291:H394–H402.

Cinthio M, Jansson T, Persson HW, Lindström K. Non-invasive measurements of longitudinal strain of the arterial wall. Proc IEEE Int Ultrason Symp 2007;570–572.

Cinthio M, Hasegawa H, Kanai H. Initial phantom validation of minute roughness measurement using phase tracking for arterial wall diagnosis non-invasively in vivo. IEEE Trans Ultrason Ferroelectr Freq Control 2011;58:853–857.

Couade M, Pernot M, Prada C, Messas E, Emmerich J, Bruneval P, Criton A, Fink M, Tanter M. Quantitative assessment of arterial wall biomechanical properties using shear wave imaging. Ultrasound Med Biol 2010;36:1662–1676.

Eriksson A, Greiff E, Loupas T, Persson M, Pesque P. Arterial pulse wave velocity with tissue Doppler imaging. Ultrasound Med Biol 2002;28:571–580.

Golemati S, Sassano A, Lever MJ, Bharath AA, Dhanjil A, Nicolaides AN. Carotid artery wall motion estimated from B-mode ultrasound using region tracking and block matching. Ultrasound Med Biol 2003;29:387–399.

Grobbee DE, Bots ML. Carotid artery intima−media thickness as an indicator of generalized atherosclerosis. J Intern Med 1994;236:567–573.

Hasegawa H, Kanai H, Hoshimiya N, Chubachi N, Koiwa Y. Accuracy evaluation in the measurement of a small change in the thickness of arterial walls and the measurement of elasticity of the human carotid artery. Jpn J Appl Phys 1998;37:3101–3105.

Hasegawa H, Kanai H, Hoshimiya N, Koiwa Y. Evaluating the regional elastic modulus of a cylindrical shell with nonuniform wall thickness. J Med Ultrason 2004;31:81–90.

Idzenga T, Holewijn S, Hansen HHG, De Korte CL. Estimating cyclic shear strain in the common carotid artery using radiofrequency ultrasound. Ultrasound Med Biol 2012;38:2229–2237.

Ito M, Arakawa M, Kanai H. Local pulse wave velocity estimated from small vibrations measured ultrasonically at multiple points on the arterial wall. Jpn J Appl Phys 2018;57 07LF14-1−07LF14-8.

Kanai H, Kawabe K, Takano M, Murata R, Chubachi N, Koiwa Y. New method for evaluating local pulse wave velocity by measuring vibrations on arterial wall. Electron Lett 1994;30:534–536.

Kanai H, Sato M, Koiwa Y, Chubachi N. Transcutaneous measurement and spectrum analysis of heart wall vibrations. IEEE Trans Ultrason Ferroelectr Freq Control 1996;43:791–810.

Kanai H, Hasegawa H, Ichiki M, Tezuka F, Koiwa Y. Elasticity imaging of atheroma with transcutaneous ultrasound—Preliminary study. Circulation 2003;107:3018–3021.

Kitamura K, Hasegawa H, Kanai H. Accurate estimation of carotid luminal surface roughness using ultrasonic radio-frequency echo. Jpn J Appl Phys 2012;51 07GF08-1−07GF08-12.

Lehmann ED, Gosling RG, Fatemi-Langroudi B, Taylor MG. Non-invasive Doppler ultrasound technique for the in vivo assessment of aortic compliance. J Biomed Eng 1992;14:250–256.

Lehmann ED, Hopkins KD, Gosling RG. Aortic compliance measurements using Doppler ultrasound: In vivo biochemical correlates. Ultrasound Med Biol 1993;19:683–710.

Luo J, Li RX, Konofagou EE. Pulse wave imaging of the human carotid artery: An in vivo feasibility study. IEEE Trans Ultrason Ferroelectr Freq Control 2012;59:174–181.

Meiburger KM, Marzola F, Zahnd G, Faita F, Loizou CP, Lainé N, Carvalho C, Steinman DA, Gibello L, Bruno RM, Clarenbach R, Francesconi M, Nicolaides AN, Liebgott H, Campilho A, Ghotbi R, Kyriacou E, Navab N, Griffin M, Panayiotou AG, Gherardini R, Varetto G, Bianchini E, Pattichis CS, Ghiadoni L, Rouco J, Orkisz M, Carotid Molinari F. Ultrasound Boundary Study (CUBS): Technical considerations on an open multi-center analysis of computerized measurement systems for intima−media thickness measurement on common carotid artery longitudinal B-mode ultrasound scans. Comput Biol Med 2022;144 105333.

Nagai Y, Hasegawa H, Kanai H. Improvement of accuracy in ultrasonic measurement of luminal surface roughness of carotid arterial wall by deconvolution filtering. Jpn J Appl Phys 2014;53 07KF19-1−07KF19-9.

Nagaoka R, Hasegawa H. Modified high-resolution wavenumber analysis for detection of pulse wave velocity using coefficient of variation of arterial wall acceleration waveforms. J Med Ultrason 2020;47:167–177.

Nilsson T, Ahlgren ÅR, Albinsson J, Segstedt S, Nilsson J, Jansson T, Persson HW, Cinthio M. A fast 2D tissue motion estimator based on the phase of the intensity enables visualization of the propagation of the longitudinal movement in the carotid artery wall. Proc IEEE Int Ultrason Symp 2013;1761–1764.

Obara Y, Mori S, Arakawa M, Kanai H. Multifrequency phased tracking method for estimating velocity in heart wall. Ultrasound Med Biol 2021;47:1077–1088.

Persson M, Ahlgren ÅR, Eriksson A, Jansson T, Persson HW, Lindström K. Non-invasive measurement of arterial longitudinal movement. Proc IEEE Int Ultrason Symp 2002;1783–1786.

Pozza RD, Pizer R, Beyerlein A, Weberru H, Oberhoffer R, Schmidt-Trucksäss A, Netz H, Haas N. Beyond intima-media-thickness: Analysis of the carotid intima−media-roughness in a paediatric population. Atherosclerosis 2016;251:164–169.

Rabben SI, Bjærum S, Sørhus V, Torp H. Ultrasound-based vessel wall tracking: an auto-correlation technique with RF center frequency estimation. Ultrasound Med Biol 2002;28:507–517.

Rafati M, Rahimzadeh MR, Moladoust H. Evaluation of atherosclerosis severity based on carotid artery intima−media thickness changes: A new diagnostic criterion. Ultrasound Med Biol 2019;45:2950–2957.

Ramnarine KV, Garrard JW, Kanber B, Nduwayo S, Hartshorne TC, Robinson TG. Shear wave elastography imaging of carotid plaques: Feasible, reproducible and of clinical potential. Cardiovasc Ultrasound 2014;12:1–8.

Rizi FY, Au J, Yli-Ollila H, Golemati S, Makūnaitė M, Orkisz M, Navab N, MacDonald M, Laitinen TM, Behnam H, Gao Z, Gastounioti A, Jurkonis R, Vray D, Laitinen T, Sérusclat A, Nikita KS, Zahnd G. Carotid wall longitudinal motion in ultrasound imaging: an expert consensus review. Ultrasound Med Biol 2020;46:2605–2624.

Saito T, Mori S, Arakawa M, Ohba S, Kobayashi K, Kanai H. Estimation of viscoelasticity of radial artery via simultaneous measurement of changes in pressure and diameter using a single ultrasound probe. Jpn J Appl Phys 2020;59 SKKE04-1−SKKE04-7.

Salles S, Chee AJY, Garcia D, Yu ACH, Vray D, Liebgott H. 2-D arterial wall motion imaging using ultrafast ultrasound and transverse oscillations. IEEE Trans Ultrason Ferroelectr Freq Control 2015;62:1047–1058.

Schmidt-Trucksäss A, Sandrock M, Cheng DC, Müller HM, Baumstark MW, Rauramaa R, Berg A, Huonker M. Quantitative measurement of carotid intima−media roughness—Effect of age and manifest coronary artery disease. Atherosclerosis 2003;166:57–65.

Shoji Y, Mori S, Arakawa M, Ohba S, Kobayashi K, Kanai H. Estimation of viscoelasticity of radial artery during flow-mediated dilatation using a single ultrasound probe based on blood pressure measurement via pulse transit time method. Jpn J Appl Phys 2021;60 SDDE03-1−SDDE03-3.

Stein JH, Korcarz CE, Hurst RT, Lonn E, Kendall CB, Mohler ER, Najjar SS, Rembold CM, Post WS. Use of carotid ultrasound to identify subclinical vascular disease and evaluate cardiovascular disease risk: A consensus statement from the American Society of Echocardiography Carotid Intima−Media Thickness Task Force endorsed by the Society for Vascular Medicine. J Am Soc Echocardiogr 2008;21:93–111.

Strotmann JM, Kvitting JPE, Wilkenshoff UM, Wranne B, Hatle L, Sutherland GR. Anatomic M-mode echocardiography: A new

approach to assess regional myocardial function—A comparative in vivo and in vitro study of both fundamental and second harmonic imaging modes. J Am Soc Echocardiogr 1999; 12:300–307.

Swillens A, Santis GD, Degroote J, Lovastakken L, Vierendeels J, Segers P. Accuracy of carotid strain estimates from ultrasonic wall tracking: A study based on Multiphysics simulations and in vivo data. IEEE Trans Med Imaging 2012;31:131–139.

Tat J, Psaromiligkos IN, Daskalopoulou SS. Carotid atherosclerotic plaque alters the direction of longitudinal motion in the artery wall. Ultrasound Med Biol 2016;42:2114–2122.

Wada T, Kodaira K, Fujishiro K, Maie K, Tsukiyama E, Fukumoto T, Uchida T, Yamazaki S. Correlation of ultrasound-measured common carotid artery stiffness with pathological findings. Arterioscler Thromb Vasc Biol 1994;14:479–482.

Yli-Ollila H, Laitinen T, Weckström M, Laitinen TM. Axial and radial waveforms in common carotid artery: An advanced method for studying arterial elastic properties in ultrasound imaging. Ultrasound Med Biol 2013;39:1168–1177.

Zahnd G, Boussel L, Marion A, Durand M, Moulin P, Sérusclat A, Vray D. Measurement of two-dimensional movement parameters of the carotid artery wall for early detection of arteriosclerosis: A preliminary clinical study. Ultrasound Med Biol 2011;37:1421–1429.

Zhang X, Kinnick RR, Fatemi M, Greenleaf JF. Noninvasive method for estimation of complex elastic modulus of arterial vessels. IEEE Trans Ultrason Ferroelectr Freq Control 2005;52:642–652.